Effect of Interlayer Spacing on the Activity of Layered Manganese Oxide Bilayer Catalysts for the Oxygen Evolution Reaction

Qing Kang,[†,‡,||] Loranne Vernisse,[†,‡,⊥] Richard C. Remsing,[†,‡,§] Akila C. Thenuwara,[†,‡] Samantha L. Shumlas,[†,‡] Ian G. McKendry,[†,‡] Michael L. Klein,[†,‡,§] Eric Borguet,[†,‡] Michael J. Zdilla,[†,‡] and Daniel R. Strongin*[,†,‡]

[†]Department of Chemistry, Temple University, Beury Hall, 1901 North 13th Street, Philadelphia, Pennsylvania 19122, United States

[‡]Center for the Computational Design of Functional Layered Materials (CCDM), Temple University, Philadelphia, Pennsylvania 19122, United States

[§]Institute for Computational Molecular Science, Temple University, SERC, 1925 North 12th Street, Philadelphia, Pennsylvania 19122, United States

S Supporting Information

ABSTRACT: We investigated the dependence of the electro-catalytic activity for the oxygen evolution reaction (OER) on the interlayer distance of five compositionally distinct layered manganese oxide nanostructures. Each individual electro-catalyst was assembled with a different alkali metal intercalated between two nanosheets (NS) of manganese oxide to form a bilayer structure. Manganese oxide NS were synthesized via the exfoliation of a layered material, birnessite. Atomic force microscopy was used to determine the heights of the bilayer catalysts. The interlayer spacing of the supported bilayers positively correlates with the size of the alkali cation: NS/Cs$^+$/NS > NS/Rb$^+$/NS > NS/K$^+$/NS > NS/Na$^+$/NS > NS/Li$^+$/NS. The thermodynamic origins of these bilayer heights were investigated using molecular dynamics simulations. The overpotential (η) for the OER correlates with the interlayer spacing; NS/Cs$^+$/NS has the lowest η (0.45 V), while NS/Li$^+$/NS exhibits the highest η (0.68 V) for OER at a current density of 1 mA/cm^2. Kinetic parameters (η and Tafel slope) associated with NS/Cs$^+$/NS for the OER were superior to that of the bulk birnessite phase, highlighting the structural uniqueness of these nanoscale assemblies.
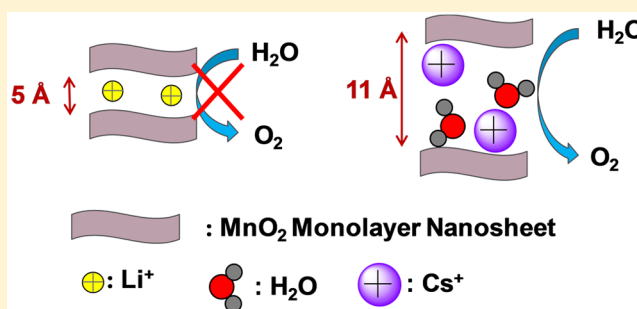
1. INTRODUCTION

As one of the most vital solar energy conversion reactions, the direct photo(electro)chemical splitting of water into H$_2$ and O$_2$ has attracted extensive attention.[1,2] Water oxidation is typically considered to be the bottleneck in artificial photosynthetic systems designed for water splitting.[3] The development of efficient oxygen evolution reaction (OER) catalysts is needed to address the challenge of solar fuel production for storing renewable energy in the form of chemical fuels.[4] To date, the most robust and efficient OER catalysts are precious metal oxides (e.g., RuO$_2$ and IrO$_2$).[5−7] Their scarcity and prohibitive cost, however, renders their use impractical for large-scale applications. Thus, it is important to develop inexpensive and highly active OER catalysts. Manganese oxides due to their natural abundance, low toxicity, and compositional similarity to nature's water splitting inorganic cluster, the oxygen-evolving complex of photosystem II, have captured the attention of researchers.[8,9]

Manganese oxides exhibit over 20 polymorphs, each typically having multivalent Mn oxidation states and nonstoichiometric compositions, making them more complicated than simple oxides.[9,10] The catalytic activity of manganese oxide also relies heavily on the phase's chemical composition, crystallographic structure, morphology, and microscopic structure.[9,11−14] For example, prior studies have suggested that the OER can take place in the interlayer region of the layered δ-MnO$_2$[15] or in the tunnel structures that make up the α-phase of MnO$_2$.[9] The layered MnO$_2$, birnessite, offers an opportunity to understand how the catalytic activity of a manganese oxide material is controlled by its microstructure. In particular, birnessite can be exfoliated, and the resulting nanosheets (NS) can be used to assemble a manganese oxide layered material one layer at a time. Prior studies have shown that this can be accomplished by using the positively charged molecule, polyethyleninimine (PEI), to bind the negatively charged layers together, one layer at a time.[16,17] It was proposed that the anisotropic features of the NS could be potentially useful for applications including cosmetics,[18] electronics,[19] and catalysis.[20]

In the present study, we build on prior research and investigate manganese oxide catalysts assembled from NS as electrocatalysts for the OER. In particular, we investigate bilayer manganese oxide catalysts that we assemble from manganese oxide NS. Unlike prior studies where PEI was used to bind sheets together, we individually incorporate five different alkali metals between the two manganese oxide sheets via a solution phase preparatory method. By using different alkali metal cations (Li^+, Na^+, K^+, Rb^+, and Cs^+), we control the interlayer spacing in the bilayer structures. Complementary molecular dynamics (MD) simulations are used to shed light on the origins of the experimentally determined spacings. Constructing bilayers with varying interlayer spacing allows us to understand how interlayer spacing in a layered material affects its activity for the OER. In the K^+ circumstance, we also assembled manganese oxide catalysts up to 21 layers high and studied the OER activity as a function of layer number. Atomic force microscopy (AFM) was used to determine the height of the manganese oxide bilayers as a function of the incorporated alkali metal cation. The electrocatalytic activity of the few layer manganese oxide catalysts for the OER was a strong function of the nature of the intercalated alkali metal.

2. RESULTS AND DISCUSSION

Morphology and Structure of Few-Layer Manganese Oxide. Sheets of manganese oxide were assembled into few-layer structures using an electrostatic self-assembly technique (Scheme 1). The strategy was similar to that used in prior

Scheme 1. Assembly of NS into Few-Layer Materials
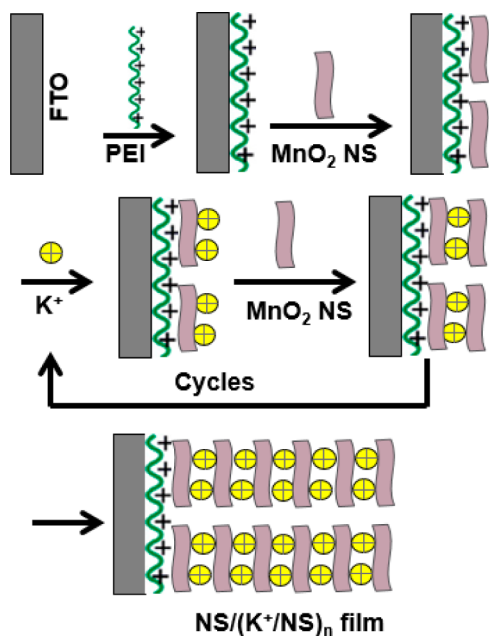
research[16] where the positively charged polycation, PEI, was used to aid in the sequential stacking of negatively charged manganese oxide NS on a fluorinated tin oxide (FTO) slide. In the current research, PEI was used only to bind the bottom-most NS to the FTO substrate. After the first NS was electrostatically fixed to the FTO, the resulting NS/FTO slide was dipped into an alkali cation containing solution (containing either Li^+, Na^+, K^+, Rb^+, or Cs^+), washed in DI water, dried with an air flow, and then dipped for a second time in the NS

suspension. This particular dipping sequence resulted in bilayer manganese oxide structures with alkali cation in the interlayer region. We use the notation, NS/(alkali cation)/NS, to refer to the particular bilayer structure henceforth.

In the K^+-circumstance, not only was a bilayer structure formed, but further cycling produced 6, 11, and 21 layer structures. These layered structures ranged in color from a light-brown to deep brown color (Figure 1a). The growth of
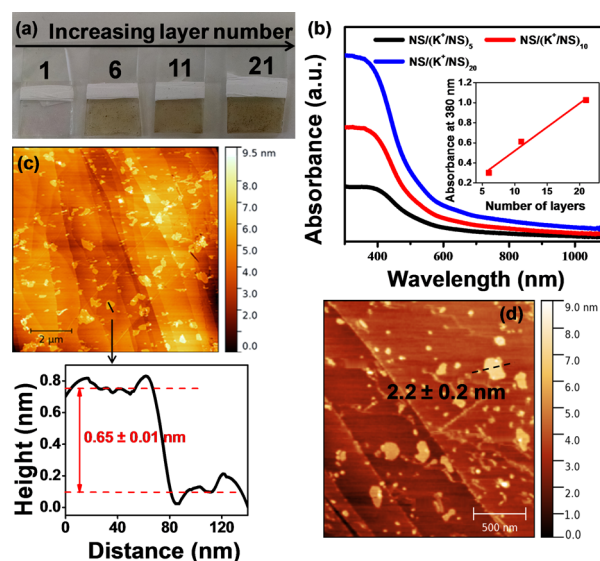

Figure 1. (a) Photograph of NS/(K^+/NS)$_n$ samples with different layer numbers (n = 1, 6, 11, and 21; n = NS − 1); (b) UV−vis absorption spectra of multilayer NS/(K^+/NS)$_n$ films; (c) AFM image of a NS on HOPG. The height of a single NS is 0.65 nm. (d) AFM image of bilayer NS/K^+/NS sample film on HOPG.

these layered materials was followed with UV−vis absorption spectroscopy (Figure 1b). The absorbance of the samples showed a linear dependence on the deposited number of layers (inset in Figure 1b) consistent with layer-by-layer growth. Transmission electron microscopy (TEM) and AFM were used to characterize the morphology of the as-grown few-layer materials. TEM showed that the NS had lateral dimensions between 50 and 100 nm (Figure S1).

To perform AFM analysis, the few-layer materials were assembled on highly ordered pyrolytic graphite (HOPG), which provided a much flatter and featureless supporting substrate than FTO. The measured thickness of monolayer NS was found to be 0.65 ± 0.10 nm (Figure 1c). We also characterized the morphology of the bilayer NS/K^+/NS film (Figure 1d). The height of the bilayer was found to be 2.2 ± 0.2 nm. Assuming a NS height of 0.65 nm, we calculate that the interlayer distance between the two sheets is 0.9 ± 0.2 nm. This value is larger than the 0.7 nm interlayer spacing that is typically associated with bulk birnessite.[21] We emphasize that by using AFM analysis we determined that bilayer structures could not be formed without alkali in the interlayer. We presume that without alkali cations in the interlayer, electrostatic repulsion between the negatively charged NS prevents bilayer formation. AFM-derived data along with those for the other four alkali metals are summarized in Figure 2. We point out that AFM did identify minority amounts of monolayer and multilayer NS, in addition to the predominant NS/(alkali cation)/NS structures (Figures S2 and S3). Interlayer spacings inferred from the AFM analysis (Figure S4 and S5) were calculated to be 0.5 ± 0.15,
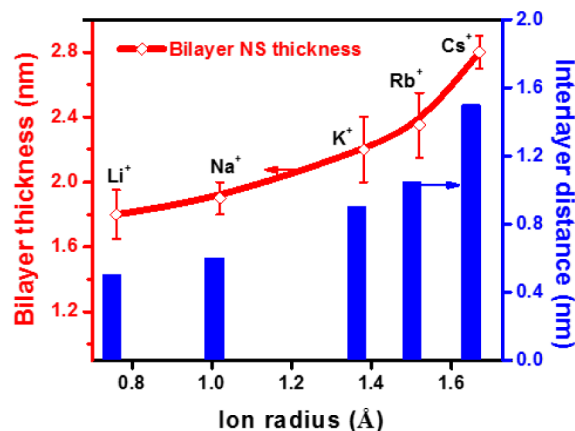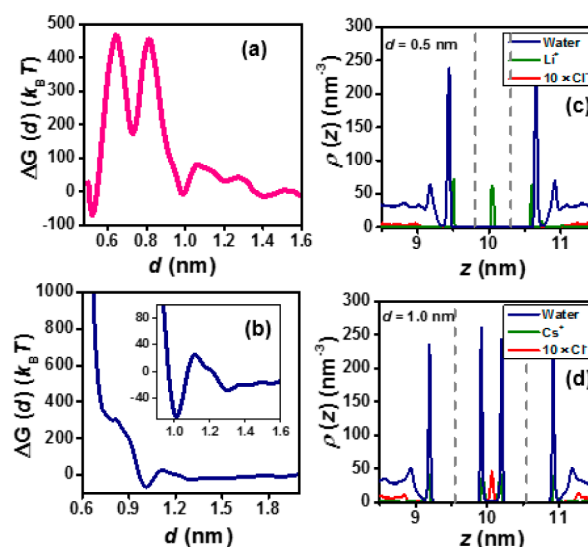
Figure 2. Bilayer NS thickness and interlayer distance obtained by AFM. Bilayers were prepared at room temperature and received no heating prior to AFM imaging.

Figure 3. Free energy as a function of the interlayer distance d for two MnO_2 NS (a) in 1 M LiCl and (b) 1 M CsCl. The inset in (b) depicts the enlarged range from 0.9 to 1.6 nm, highlighting the relevant free energy minima and maxima. (c) Number densities of water, Li^+, and Cl^- ions for an interlayer distance of 0.5 nm. Note that only Li^+ ions are between the sheets. (d) Number densities of water, Cs^+, and Cl^- ions for interlayer distance of 1.0 nm. Dashed lines indicate the positions of the Mn layers in the sheets.

0.6 ± 0.08, 0.9 ± 0.08, 1.05 ± 0.2, and 1.5 ± 0.09 nm for NS/Li^+/NS, NS/Na^+/NS, NS/K^+/NS NS/Rb^+/NS, and NS/Cs^+/NS, respectively. For the NS/K^+/NS, NS/Rb^+/NS, and NS/Cs^+/NS bilayer systems, the interlayer spacing is larger than the 0.7 nm spacing associated with bulk birnessite, suggesting that the bilayer likely can accommodate more water than the bulk birnessite structure. The reason for the dependence of the interlayer spacing on alkali metal is uncertain. The size of the ion can, of course, play a role and on a qualitative level the interlayer spacing increase does follow the increase in alkali metal diameter as one goes down the alkali series from Li^+ to Cs^+. However, the alkali metal diameter can account for only 10% of the interlayer spacing. To further investigate the origins of the interlayer distances in these materials, we performed MD simulations.

We first focus on the abnormally small interlayer distance of 0.5 nm obtained in the case of Li^+. Interestingly, this 0.5 nm interlayer distance, characteristic of the NS/Li^+/NS system, is similar to the interlayer spacing of dehydrated bulk birnessite where only alkali metal is present.[22] Hence, it may be that the strong interaction of Li^+ with the NS leads to the loss of water from the interlayer region accounting for the short interlayer distance. The existence of such a dry state is supported by the potential of mean force (PMF) shown in Figure 3a, which contains a free energy minimum near an interlayer distance of d = 0.5 nm, while the normal birnessite-like structure is a local minimum surrounded by large barriers. The density of atomic sites shows that the interlayer is dry (Figure 3c). There is no water density in the interlayer region but there is significant Li^+ density. The formation of this structure is favored by strong direct Li^+-NS interactions and occurs when this energy outweighs the free energy change upon water penetration with an accompanying increase in the interlayer spacing.

Direct interactions between the alkali and the charged sheets progressively weaken as one moves from K^+ to Cs^+ and may play a role in the interlayer distance increase. It is important to mention that buserite, another manganese oxide mineral, contains octahedrally Mn-coordinated sheets similar to birnessite. But in contrast to birnessite, buserite has an interlayer spacing close to 1 nm.[23] This increased interlayer spacing of buserite is attributed to two layers of water in the interlayer region, and indeed, buserite can be converted into birnessite through heating and dehydration. Thus, we anticipate that the K^+ bilayer system is similar to that of buserite, and the

system is trapped in a local free energy minimum which requires heating and dehydration to overcome a barrier into the birnessite-like state.

The Cs^+ bilayer system has a significantly larger experimentally determined interlayer spacing of 1.5 ± 0.09 nm. Such a spacing can fit roughly 3−4 layers of water in the interlayer region. The PMF for the Cs^+ system shows two free energy minima, a global minimum at d = 1 nm, which is separated from a local minimum near d = 1.4 nm by a large free energetic barrier nearly 50 $k_B T$ higher than this local minimum (Figure 3b). Thus, the experimentally obtained systems may be in the local free energy minimum and would require additional work, like dehydration, to reach the global minimum. Indeed, heating the samples to 100 °C enables this barrier to be overcome and the interlayer distance reduces to 1.1 nm (discussed below), close to the minimum free energy state predicted by simulation and shown in Figure 3b.

The origin of the minima is related to the adsorption of Cs^+ to the MnO_2 NS. The direct interaction between Li^+ and the negatively charged NS is the strongest of the alkalis, because Li^+ has the highest charge density. However, solvent effects result in Cs^+ being driven most to adsorb to the NS surface, as shown in Figures S6−S8. This strong adsorption of Cs^+ to the surface results in the formation of tightly bound "Stern" layers of cations on the MnO_2 sheets, illustrated by the density profiles shown in Figure 3d and Figure S9. As expected, the Stern layer is followed by a diffuse layer composed of cations and anions. As two NS approach one another, the first (local) minimum corresponds to the sharing of diffuse layers by the two surfaces (Figure S9). The free energetic barrier corresponds to removing the diffuse layers, while the global minimum in the PMF corresponds to two intact Stern layers separated by water and a layer of anions (Figure 3d). The high adsorption of Cs^+ neutralizes and screens the charge on the MnO_2 sheets (Figure S6). The neutral but polar Cs^+/MnO_2 sheets are then separated

by a layer of water, stabilizing the interlayer distance of 1 nm. Finally, we note that the PMF does display a small shoulder at the distance indicative of a birnessite-like bilayer at 1 M CsCl (near 0.7 nm), which may become a local minimum under different conditions. The structure at this distance corresponds to a single layer of water and cations bridging two MnO_2 NS.

Based on interlayer spacing, the bilayer materials assembled using K^+, Rb^+, and Cs^+ have no direct connection to bulk 3D layered birnessite phases. All of these bilayers have an interlayer spacing that is larger than birnessite (0.7 nm) or buserite (1 nm). Hence, they appear to be unique to these particular nanobilayer structures. This contention is emphasized by the results of experiments that assembled the NS back into bulk birnessite using the different alkali metals. In short, we individually added 5 mM LiCl, NaCl, KCl, RbCl, and CsCl into five separate NS suspensions. After addition of the alkali metal, the NS precipitated out of solution, and the particulate (identified as birnessite by X-ray diffraction (XRD), Figure S10) was separated and collected by centrifugation. Analysis of the (001) reflections for the different alkali metal cation birnessites showed that the interlayer spacing changed from 0.73 nm for Li^+/birnessite to 0.77 nm for Cs^+/birnessite. While the trend in interlayer spacing for the different alkali metals was similar to what was observed in the bilayer materials, the magnitude of change was far less for these bulk birnessite materials. This experimental observation again emphasizes that these particular bilayer materials are unique structures that cannot be directly associated with the birnessite (or buserite) phase.

Electrochemical Activity of Bilayers for OER. The electrocatalytic activity of the bilayer structures was investigated in the context of the OER. It is important to point out that to obtain the largest currents during electrochemical experiments, bilayer samples were heated to 100 °C on FTO (see the Experimental Section). AFM analysis of similar bilayer samples supported on atomically flat mica substrates showed a decrease in interlayer distance after heat treatment to 100 °C relative to the bilayers prepared at room temperature (AFM-derived bilayer thicknesses shown in Figure S11). In this circumstance, the AFM-derived interlayer spacings were 0.5 ± 0.15, 0.5 ± 0.08, 0.7 ± 0.2, 0.9 ± 0.2, and 1.1 ± 0.09 nm for NS/Li^+/NS, NS/Na^+/NS, NS/K^+/NS, NS/Rb^+/NS, and NS/Cs^+/NS, respectively. After heating, the interlayer distances suggest that NS/Li^+/NS and NS/Na^+/NS are largely dehydrated, while NS/K^+/NS, NS/Rb^+/NS, and NS/Cs^+/NS are hydrated, with perhaps NS/Cs^+/NS containing up to two layers of water in analogy with buserite.

Figure 4 displays polarization curves along with Tafel plots for the different alkali metal intercalated NS bilayer systems at oxidizing potentials. Also shown in the plot are polarization curves for bulk IrO_2 and RuO_2. The order of increasing overpotential (η) at a current density of 5 mA/cm^2 for the OER is as follows: NS/Cs^+/NS (η = 0.613 V) < NS/Rb^+/NS (η = 0.662 V) < NS/K^+/NS (η = 0.709 V) < NS/Na^+/NS and NS/Li^+/NS. The latter two systems were particularly inactive for water oxidation, and a current density of 5 mA/cm^2 could not be achieved with these two systems at the potentials used to obtain the polarization curves. In addition to the η value, another metric for the OER activity of electrocatalysts is the Tafel slope: the lower the slope the higher the activity gain per amount of applied overpotential. Based on an analysis of the Tafel slopes for the different bilayer systems, the NS/Cs^+/NS system associated with a Tafel slope of 101 mV/dec (Figure
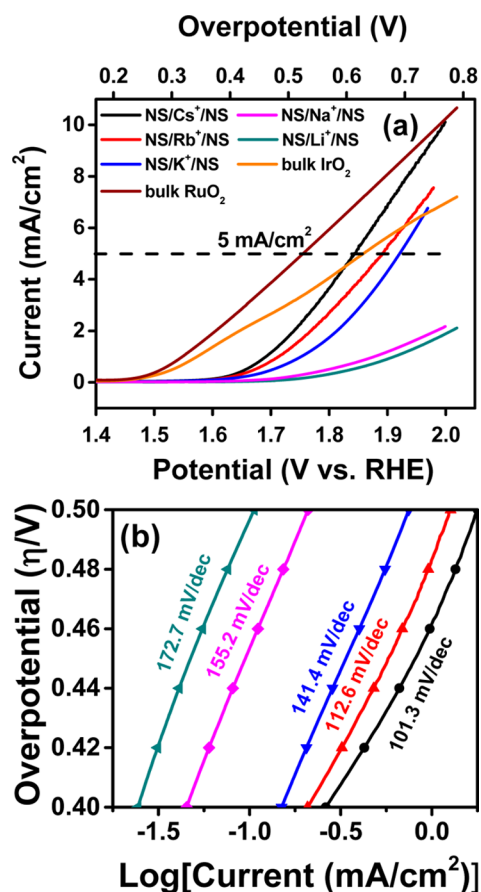
Figure 4. (a) Polarization curves for NS/M^+/NS (M^+ = Li^+, Na^+, K^+, Rb^+, and Cs^+) and NS/PEI/NS. (b) Corresponding Tafel plots of the different bilayer materials.

4b) was significantly lower than the Tafel slope associated with bulk K-birnessite (243 mV/dec).[21] Figure 5 plots the η values
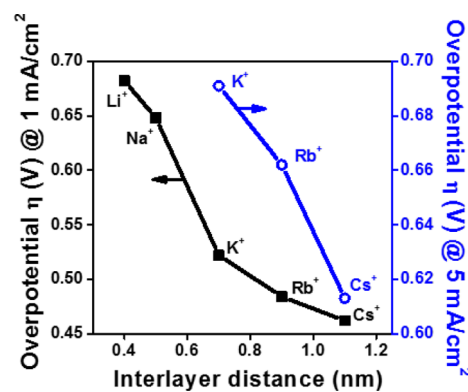
Figure 5. Overpotential for the OER vs interlayer distance plot for NS/M^+/NS (M^+ = Li^+, Na^+, K^+, Rb^+, and Cs^+) films. AFM measurements of the bilayers were carried out after heating to 100 °C.

for the different bilayer systems (at a current density of 1 and 5 mA/cm^2) as a function of interlayer spacing. In general, there is a drop in η with increasing interlayer spacing. The interlayer spacing of NS/Li^+/NS is similar to that associated with dehydrated birnessite (~0.5 nm), likely suggesting that the inactivity of this bilayer system is the inability of water to efficiently access reactive surface sites in the interlayer region. This is supported by the dry interlayer region observed in our

MD simulations. Hence, for NS/Li$^+$/NS, we suggest that the OER is primarily limited to the outermost surface of the bilayer. The continuing drop in the value of η as one systematically increases the size of the alkali metal likely occurs in large part to the increasing amount of water that can be accommodated in the interlayer region. In short, diffusion of water in and out of the interlayer regions would be expected to be enhanced with increasing interlayer distance.

We also acquired polarization curves for bilayer deposited on FTO that were kept at room temperature at all times (were not heated to 100 °C). The interlayer distances of these films are presented in Figure 2. The polarization curves for these systems are exhibited in Figure S12. The electrochemical current achieved from these catalysts was markedly lower than those bilayers that were heated to 100 °C. We believe the important experimental observation, however, is that the trend in activity with interlayer distance was the same as for the heated samples. For example, at a current density of 2 mA/cm^2, the experimentally determined η values were 0.70 V (NS/Cs$^+$/NS) < 0.74 (NS/Rb$^+$/NS) < 0.76 (NS/K$^+$/NS) < 0.80 (NS/Na$^+$/NS) < 0.83 (NS/Li$^+$/NS). These particular data are plotted in Figure S12. We suspect that the lower activity for these bilayers is likely due to the lack of direct contact between the bilayer and FTO substrate. A layer of water between the FTO and bilayer may exist in the absence of heating, resulting in a poor electrical contact.

A recent study brings forward another reason (other than change in interlayer spacing) for the correlation between OER and alkali cation intercalation in our bilayer systems.[24] In this prior study, it was shown that the OER electrocatalytic activity of an electroplated MnO$_x$ catalyst depended strongly on the nature of the electrolyte in solution. In particular, the overpotential for the OER for the MnO$_x$ film was the highest in the presence of LiOH and the lowest in the presence of CsOH electrolyte. It was proposed that the strong binding of Li$^+$ to the hydroxylated active sites for the OER on the film blocked the reaction. It was also surmised, based on X-ray absorption measurements, that Li$^+$ stabilized lower oxidation states of Mn (e.g., Mn(II)) that were not active for the OER. While we do not have data that investigated the oxidation state of Mn in the presence of the alkali metals, the contention that Li$^+$ binds strongly to the manganese oxide sheets is consistent with the small interlayer spacing associated with NS/Li$^+$/NS, although the surfaces studied here are not hydroxylated.

Electrochemical Activity of NS/(K$^+$/NS)$_n$ for OER as a Function of Layer Number. For the K$^+$/NS system, we extended our reactivity studies to catalysts containing more than two layers of NS. Figure 6a displays polarization curves for NS/(K$^+$/NS)$_n$ systems having 2 ($n = 1$), 6 ($n = 5$), 11 ($n = 10$), 16 ($n = 15$), and 21 ($n = 20$) layers of MnO$_2$. Also shown are polarization curves for control systems: a single NS (not layered) on FTO, FTO with a PEI layer, and clean FTO. These latter three systems show a much lower activity than the NS/(K$^+$/NS)$_n$-layered systems and are not discussed further. The layered systems show a decreasing η with increasing layer number, and this dependence is plotted in Figure 6b. The values of η to reach a current density of 5 mA/cm^2 are 709, 652, 610, 551, and 615 mV for the 2-, 6-, 11-, 16-, and 21-layer K$^+$/NS, respectively (Figure 6b). It is useful to evaluate the Tafel slope and exchange current densities of the different layered systems. Tafel plots are fit to the equation, $\eta = a + b \log J$, where b is the Tafel slope for a particular layered system, J is the current density, and when $\eta = 0$, J is the exchange current
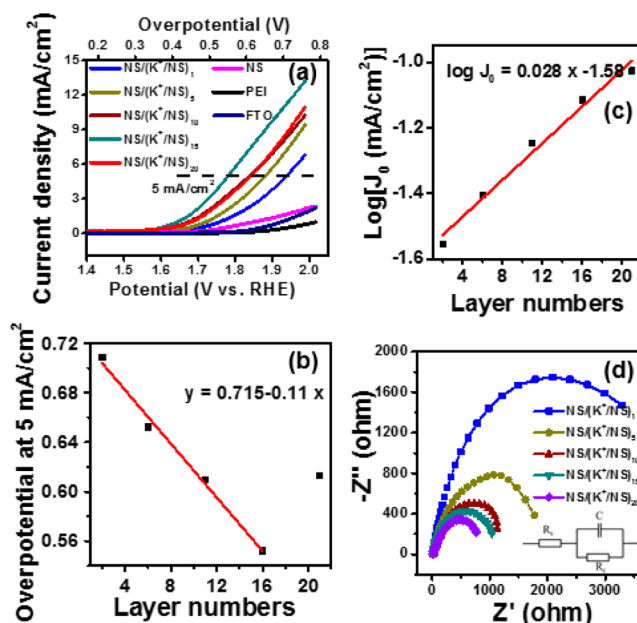
Figure 6. (a) Polarization curves, (b) overpotential at 5 mA/cm^2, (c) exchange current density, and (d) EIS of multilayer NS/(K$^+$/NS)$_n$ films with different K$^+$/NS layer cycles. The inset in (d) is the equivalent circuit used to fit the experimental data.

density (J_0). This analysis shows that all of the NS/(K$^+$/NS)$_n$ films have Tafel slopes in the range of 141−171 mV/dec (Figure S13). The similarity of the Tafel slopes suggests that the mechanism for OER does not change with the layer number. Of note, however, is that the Tafel slope of these layered systems is lower than that of the bulk birnessite (243 mV/dec).[21] Figure 6c shows that the exchange current density, J_0, increases with layer number: increasing by a factor of 1.07 for every layer increment. The amount of Mn and K in the NS/(K$^+$/NS)$_n$ films were determined by inductively coupled plasma optical emission spectrometry (ICP-OES) (Figure S14). The catalytic activity of NS/(K$^+$/NS)$_n$ as a function of the layer number is also illustrated by a comparison of turnover frequencies (TOF) and mass activities (Table 1). The electrochemically active surface area (ECSA) and the roughness factor (RF) are also summarized in Table 1. NS/(K$^+$/NS)$_{15}$ exhibits a water oxidation TOF (at $\eta = 0.45$ V) of 0.022 s^{-1}, which is higher than other NS/(K$^+$/NS)$_n$ films and is also 10-fold higher than the TOF previously reported for bulk manganese oxides.[9,21] The ECSA shows that the number of active sites increase gradually with increasing layer number (to 16), beyond which the ECSA remains nearly constant. This leads to a lowering of the mass activity for the thickest film studied. The reason for this behavior is uncertain, but may be due to structural changes that start to make interlayer reaction sites less accessible. The increasing exchange current density with the layer number is consistent with the notion that the OER occurs, at least in part, within the interlayer region of the layered materials, although this increase being attributed to the increasing amount of edge sites cannot be ruled out. Results obtained from the bilayer systems, however, show that with increasing interlayer spacing there is a lowering of the overpotential (Figure 5). This suggests that edge site catalysis is likely not the primary factor. Also an AFM analysis on bilayer systems suggests that lateral sizes are independent of the interlayer cation. This analysis suggests that the amount of edge

Table 1. Summary of Catalytic Activities and Atomic Ratios from ICP-OES

catalyst	K/Mn atomic ratio	TOF (s^{-1}) at η = 0.45 V	mass activity (A/g) at η = 0.45 V	ECSA (cm^2)	RF	C_{DL} (mF/cm^2)	R_s/Ω	R_c/Ω
NS/$(K^+/NS)_1$	0.192	0.017	76.1	3.3	3.33	0.133	20.1	4199
NS/$(K^+/NS)_5$	0.253	0.016	69.9	9.5	9.48	0.379	18.9	1958
NS/$(K^+/NS)_{10}$	0.235	0.018	81.5	16.9	16.9	0.674	19.6	1339
NS/$(K^+/NS)_{15}$	0.259	0.022	96.8	22.8	22.8	0.913	19.3	1084
NS/$(K^+/NS)_{20}$	0.264	0.018	79.1	22.1	22.1	0.886	19.1	1045

in a particular bilayer system does not depend on the nature of the interlayer alkali metal cation (Figure S15).

Finally, we conducted electrochemical impedance spectroscopy (EIS) on the NS/$(K^+/NS)_n$ as a function of layer number. Figure 6d shows typical Nyquist plots for the various NS/$(K^+/NS)_n$ films obtained at 1.62 V (reversible hydrogen electrode (RHE) scale). It is found that the arc sizes are linearly dependent on the layer number of K^+/NS. All impedance spectra are fitted using an equivalent RC circuit model, as shown in the inset of Figure 6d. Table 1 summarizes the impedance parameters obtained by fitting the experimental data. No major differences in the resistivity of the electrolyte between the working and reference electrode (R_s) of the five different electrodes were found. The charge transfer resistivity of the redox reaction (R_c) of NS/$(K^+/NS)_{15}$ (1084 Ω), is lower than that found for NS/$(K^+/NS)_{10}$ (1339 Ω), NS/$(K^+/NS)_5$ (1958 Ω), and NS/$(K^+/NS)_1$ (4199 Ω). These measurements suggest that the charge transfer resistance decreases with the layer number. However, if the layer number is increased further, the thick multilayer film starts to hinder charge transfer, resulting in the R_c for NS/$(K^+/NS)_{20}$ being similar to R_c for NS/$(K^+/NS)_{15}$.

Stability of NS/K^+/NS Film for OER. Stability is another crucial factor to be considered for electrocatalysts. Figure S16 shows enhanced stability of NS/K^+/NS film relative to bulk birnessite. After 100 potential cycles, the LSV curves of the NS/K^+/NS film keeps 71% activity of the initial one, while the bulk birnessite decreases to 0.8 mA/cm^2 at +2.0V_{RHE} (52% activity of the initial one). This suggests that the ultrathin film expresses a strong bonding between the NS, which likely enables effective electron collection and fast electron transfer. Furthermore, after electrocatalytic testing for 1 h, the UV−vis absorption of the NS/K^+/NS film showed that 78.4% of the initial film was still present on the electrode (Figure S17).

3. CONCLUSION

The electrocatalytic activity of bilayer manganese oxide catalysts for the OER shows a strong dependence on the nature of the intercalated alkali metal. In particular, the interlayer spacing can be controlled by the choice of the alkali metal due to an interplay of direct ion-NS interactions and solvent-induced effects. In the case of a large alkali metal cation, such as Cs$^+$, the interlayer spacing is larger than in the bulk layered manganese oxides, such as birnessite and buserite. In this regard, the bilayer assemblies are unique nanoscale structures that show enhanced reactivity toward the OER compared to bulk manganese oxide phases. We anticipate that our methodology for enhancing catalytic activity is general and suggest that it may be possible to form other layered structures at the nanoscale that have no bulk analogue but show enhanced catalytic activity for the OER due to unique structural properties.

4. EXPERIMENTAL SECTION

Synthesis of MnO$_2$ Nanosheets. K-birnessite was synthesized by the protocol of McKenzie.[25] Hydrochloric acid (HCl, 4 M, 50.0 mL) was dropwise added to a KMnO$_4$ solution (0.200 M, 250 mL) at 80 °C. Heating was continued at 80 °C for an additional 0.5 h after the addition of the acid was complete. The resulting solution was aged for 15 h at 50 °C, after which time the solid precipitate was collected and washed with water via vacuum filtration. XRD (Figure S13) of the obtained product agreed with that reported for K-birnessite in previous literature.[24]

The K$^+$ ions in the interlayer of the birnessite were exchanged for protons by stirring the material in an aqueous HNO$_3$ (0.1 M) for 2 days. The product was isolated by centrifugation and washed with water until the pH of the supernatant was 6−7. The product was subsequently dried in air.

Exfoliation of the proton-exchanged material was performed using an aqueous solution of tetra-n-butylammonium hydroxide (TBA$^+$OH$^-$; Aldrich Chemical Co., 40 wt % in H$_2$O) at room temperature. After the suspension was shaken for 10 days, TBAOH in solution was isolated from the particles by centrifugation at 14000 rpm for 15 min. The sediment was collected and washed with water and ethanol. The purified MnO$_2$ NS were redispersed in water to form a colloidal suspension. The component that did not become exfoliated was separated from the solution by centrifugation at 8000 rpm for 15 min. The resulting supernatant (colloidal suspension) obtained in this way contained well-dispersed exfoliated NS of manganese oxide.

Assembly of NS into Few-Layer Materials. Layered manganese oxide assemblies were fabricated by applying the layer-by-layer assembly procedure (Scheme 1). The substrate, FTO, was first cleaned by ultrasonic washing in acetone and water. FTO was precoated with PEI by immersion in an aqueous PEI solution (2.5 g/L) for 1 min. After rinsing with water and drying with a dry air, the PEI-primed substrate was then immersed in the colloidal suspension (2.85 mM) of manganese oxide NS for 1 min. This exposure was followed by a thorough washing with pure water and drying to obtain an ultrathin NS layer. The film was then immersed in an alkali metal cation containing solution (5 mM, derived from the corresponding chloride salt) for 1 min and then was rinsed with water and dried. The resulting NS with adsorbed alkali metal was dipped in the NS containing solution to form the bilayer with intercalated alkali metal. Repeated cycling was carried out to assemble NS/$(K^+/NS)_n$ materials (n = 1, 5, 10, and 15). The resulting few-layer material was kept at 100 °C overnight. We also prepared few layer materials where the heating step was eliminated and drying at a room temperature was used. Results for both circumstances are reported on this work.

Preparing the Bulk Birnessite Electrode. The bulk birnessite electrode was prepared by drop casting 100 µL of catalyst ink solution on a FTO (1 cm × 1 cm) plate. The ink solution was prepared as follows: 3 mg of bulk birnessite and 7 mg of carbon (VulcanXC-72) were dispersed in 1 mL of 2-propanol and 50 µL of Nafion solution (5% in alcohol; Ion Power Inc.). The resulting mixture was sonicated for 60 min to form a suspension.

Structural Characterization. XRD data were acquired on a Bruker Kappa APEX II DUO diffractometer using Mo Kα (0.71 Å) radiation from a sealed molybdenum tube with a TRIUMPH monochromator. In this contribution, XRD was carried out on synthetic birnessite formed by assembling the material from the aggregation of NS in solution. This preparation procedure involved adding 10 mL of an alkali metal ion containing solution (5 mM) to a colloidal suspension (2.85 mM Mn) of NS. The resulting birnessite

precipitate was centrifuged, washed with water, and dried in air. TEM images were collected using a JEOL JEM-1400 microscope operating at 120 kV. Elemental analysis was performed using a Thermo Scientific iCAP 7000 Series ICP-OES. Ultraviolet–visible (UV–vis) spectra were recorded using a Thermo Scientific Evolution-201 spectrophotometer.

Electrochemical Measurements. Electrochemical characterization of the various layered materials was performed in 1 M KOH using a CH Instrument electrochemical analyzer (model CHI660E), a Pt-sheet counter electrode, an Ag/AgCl (saturated KCl) reference electrode, and an FTO (1 cm × 1 cm) working electrode (coated with the layered material of interest). The measured potentials vs the Ag/AgCl were converted to the RHE scale via the Nernst equation[15]

$$E_{RHE} = E_{Ag/AgCl} + 0.059pH + E°_{Ag/AgCl} \quad (1)$$

where E_{RHE} is the converted potential vs RHE, $E_{Ag/AgCl}$ is the experimental potential measured against an Ag/AgCl reference electrode, and $E°_{Ag/AgCl} = 0.1976$ V at 25 °C. The electrocatalysis was measured using linear sweep voltammetry (LSV) with a scan rate of 10 mV/s. Cyclic voltammetry (CV) was performed in a range of +0.02 to +2.02 V (vs RHE) at a scan rate of 100 mV/s. EIS was obtained at +1.62 V (vs RHE). The amplitude of the sinusoidal wave was 5 mV and the frequency range examined was 100 kHz to 1 Hz. All impedance spectra were fitted using an equivalent RC circuit model (inset in Figure 6d). R_s is the resistivity of the electrolyte between the working and reference electrodes, R_c is the charge transfer resistivity of the redox reaction, and C is a capacitance in parallel with the R, which is analogous to the double-layer charging capacity of the solid–liquid junction.

Calculation Method. The mass activity and TOF of the catalysts were calculated as follows:[21]

$$mass\ activity = J/m \quad (2)$$

$$turnover\ frequency\ (TOF) = J \times A/4nF \quad (3)$$

Here, J is the measured current density (mA/cm^2) at $\eta = 0.45$ V, m is the catalyst loading (g) determined by ICP-OES, A is the geometric area (cm^2) of the FTO electrode, F is the Faraday constant (96500 C/mol), and n is the mole number of the coated catalysts.

The ECSA for each system was estimated from the electrochemical double-layer capacitance (C_{DL}) of the catalytic surface.[2] The electrochemical capacitance was determined by measuring the non-Faradaic capacitive current associated with double-layer charging from the scan-rate dependence of cyclic voltammograms.[2] The ECSA of a catalyst sample is calculated from the C_{DL} according to eq 4

$$ECSA = C_{DL}/C_s \quad (4)$$

where C_s is the specific capacitance of the sample or the capacitance of an atomically smooth planar surface of the material per unit area under identical electrolyte conditions. For our estimates of surface area, we use general specific capacitances $C_s = 0.040$ mF/cm^2 in 1 M KOH based on typical reported values.[2]

The RF was calculated by taking the estimated ECSA and dividing by the geometric area of the electrode (1 cm^2). The ECSA and RF values for NS/(K$^+$/NS)$_n$ multilayer films are displayed in Table 1.

AFM Experiments. Imaging was performed with an Agilent 5500 AFM (Agilent Technologies, AZ) in tapping mode using conical tips with aluminum reflex coating from Aspire (spring constant = 50 N/m, resonant frequency = 170 kHz). The one- to few-layer materials were assembled on HOPG or mica, which provided much flatter and featureless supporting substrates than FTO. PEI was not used prior to the material deposition in order to avoid the tip and surface contamination.

MD Simulations and Free Energy Calculations. All MD simulations included explicit representations of water, ions, and MnO$_2$ NS and were performed using GROMACS5[26] in the canonical ensemble, but in the presence of a water–vapor interface that maintains the system pressure at the coexistence pressure of water. A constant temperature of 300 K was maintained using the canonical velocity rescaling algorithm. MnO$_2$, water, and ions were modeled using the CLAYFF force field with the extended simple point charge (SPC/E) water model[27−30] following previous work. Lennard-Jones interactions were truncated at a distance of 1 nm, and the Coulomb interactions were evaluated using the particle mesh Ewald method.

The free energy as a function of the interlayer distance (d), i.e., the PMF,[31,32] was computed for two rigid MnO$_2$ NS with dimensions 3.7 × 3.1 nm^2 by performing simulations at fixed d. Each simulation was equilibrated for at least 5 ns followed by production runs at least 10 ns in duration. At each value of d, the mean force in the z-direction $\langle F_z \rangle$ was computed from the latter GROMACS production trajectories. The free energy was then obtained from integration of this mean force as a function of the interlayer distance

$$\Delta G(d) = -\int_{d_0}^{d} F_z(d')\ dd' \quad (5)$$

where d_0 is the lower bound on d and d' is a dummy variable of integration. The integral was evaluated with the trapezoid rule using a spacing of 0.01 nm. Results shown in the text were obtained with 5330 water molecules but were found to be unchanged when increasing the system size to 7376 waters, illustrating convergence with respect to system size. Similarly, multiple runs with different starting configurations were performed to ensure that the results are independent of starting configuration.

■ ASSOCIATED CONTENT

ⓢ Supporting Information

The Supporting Information is available free of charge on the ACS Publications website at DOI: 10.1021/jacs.6b09184.

> TEM and AFM images, details of MD simulations and free energy calculations for ion adsorption on a single MnO$_2$ NS, polarization curves, CV curves, Tafel plots, Mn ion and K ion concentrations with different layer numbers, XRD pattern (PDF)

■ AUTHOR INFORMATION

Corresponding Author

*dstrongi@temple.edu

ORCID ⓞ

Akila C. Thenuwara: 0000-0002-6146-9238
Michael J. Zdilla: 0000-0003-0212-2557
Daniel R. Strongin: 0000-0002-1776-5574

Present Addresses

∥(Q.K.) School of Materials Science and Engineering, Key Laboratory of Advanced Energy Storage Materials of Guangdong Province, South China University of Technology, Guangzhou 510641, P.R. China.
⊥(L.V.) Institut P', Université de Poitiers, ENSMA, SP2MI-Téléport 2, F86962 Futuroscope-Chasseneuil cedex, France.

Notes

The authors declare no competing financial interest.

■ REFERENCES

(1) Lewis, N. S.; Nocera, D. G. *Proc. Natl. Acad. Sci. U. S. A.* **2006**, *103*, 15729.

(2) McCrory, C. C.; Jung, S.; Peters, J. C.; Jaramillo, T. F. *J. Am. Chem. Soc.* **2013**, *135*, 16977.

(3) Shan, Z.; Archana, P. S.; Shen, G.; Gupta, A.; Bakker, M. G.; Pan, S. *J. Am. Chem. Soc.* **2015**, *137*, 11996.

(4) Zhou, W.; Wu, X.-J.; Cao, X.; Huang, X.; Tan, C.; Tian, J.; Liu, H.; Wang, J.; Zhang, H. *Energy Environ. Sci.* **2013**, *6*, 2921.

(5) Tilley, S. D.; Cornuz, M.; Sivula, K.; Grätzel, M. *Angew. Chem., Int. Ed.* **2010**, *49*, 6405.

(6) Fang, Y.-H.; Liu, Z.-P. *J. Am. Chem. Soc.* **2010**, *132*, 18214.

(7) McCrory, C. C.; Jung, S.; Ferrer, I. M.; Chatman, S. M.; Peters, J. C.; Jaramillo, T. F. *J. Am. Chem. Soc.* **2015**, *137*, 4347.

(8) Huynh, M.; Shi, C.; Billinge, S. J.; Nocera, D. G. *J. Am. Chem. Soc.* **2015**, *137*, 14887.

(9) Meng, Y.; Song, W.; Huang, H.; Ren, Z.; Chen, S.-Y.; Suib, S. L. *J. Am. Chem. Soc.* **2014**, *136*, 11452.

(10) Robinson, D. M.; Go, Y. B.; Mui, M.; Gardner, G.; Zhang, Z.; Mastrogiovanni, D.; Garfunkel, E.; Li, J.; Greenblatt, M.; Dismukes, G. C. *J. Am. Chem. Soc.* **2013**, *135*, 3494.

(11) Bergmann, A.; Zaharieva, I.; Dau, H.; Strasser, P. *Energy Environ. Sci.* **2013**, *6*, 2745.

(12) Devaraj, S.; Munichandraiah, N. *J. Phys. Chem. C* **2008**, *112*, 4406.

(13) Suib, S. L. *Acc. Chem. Res.* **2008**, *41*, 479.

(14) Suib, S. L. *J. Mater. Chem.* **2008**, *18*, 1623.

(15) Thenuwara, A. C.; Cerkez, E. B.; Shumlas, S. L.; Attanayake, N. H.; McKendry, I. G.; Frazer, L.; Borguet, E.; Kang, Q.; Remsing, R. C.; Klein, M. L. *Angew. Chem., Int. Ed.* **2016**, *55*, 10381.

(16) Wang, L.; Omomo, Y.; Sakai, N.; Fukuda, K.; Nakai, I.; Ebina, Y.; Takada, K.; Watanabe, M.; Sasaki, T. *Chem. Mater.* **2003**, *15*, 2873.

(17) Liu, Z.; Xu, K.; Sun, H.; Yin, S. *Small* **2015**, *11*, 2182.

(18) López-Galindo, A.; Viseras, C.; Cerezo, P. *Appl. Clay Sci.* **2007**, *36*, 51.

(19) Osada, M.; Sasaki, T. *Adv. Mater.* **2012**, *24*, 210.

(20) Tagusagawa, C.; Takagaki, A.; Hayashi, S.; Domen, K. *J. Am. Chem. Soc.* **2008**, *130*, 7230.

(21) Thenuwara, A. C.; Shumlas, S. L.; Attanayake, N. H.; Cerkez, E. B.; McKendry, I. G.; Frazer, L.; Borguet, E.; Kang, Q.; Zdilla, M. J.; Sun, J. *Langmuir* **2015**, *31*, 12807.

(22) Renuka, R.; Ramamurthy, S. *J. Power Sources* **2000**, *87*, 144.

(23) Johnson, E. A.; Post, J. E. *Am. Mineral.* **2006**, *91*, 609.

(24) Gao, Q.; Ranjan, C.; Pavlovic, Z.; Blume, R.; Schlögl, R. *ACS Catal.* **2015**, *5*, 7265.

(25) McKenzie, R. *Mineral. Mag.* **1971**, *38*, 493.

(26) Hess, B.; Kutzner, C.; van der Spoel, D.; Lindahl, E. *J. Chem. Theory Comput.* **2008**, *4*, 435.

(27) Cygan, R. T.; Liang, J. J.; Kalinichev, A. G. *J. Phys. Chem. B* **2004**, *108*, 1255.

(28) Cygan, R. T.; Post, J. E.; Heaney, P. J.; Kubicki, J. D. *Am. Mineral.* **2012**, *97*, 1505.

(29) Berendsen, H. J. C.; Grigera, J. R.; Straatsma, T. P. *J. Phys. Chem.* **1987**, *91*, 6269.

(30) Remsing, R. C.; McKendry, I. G.; Strongin, D. R.; Klein, M. L.; Zdilla, M. J. *J. Phys. Chem. Lett.* **2015**, *6*, 4804.

(31) Kirkwood, J. G. *J. Chem. Phys.* **1935**, *3*, 300.

(32) *Free Energy Calculations: Theory and Applications in Chemistry and Biology*; Springer, 2007.